1   **Feldspar alteration by disequilibrium CO_2-H_2O fluids in reservoir sandstones:**
2   **Implications for CCS**

3   Authors: Natalie. J.C. Farrell[1], Lining Yang[2], Michael. J. Flowerdew[3], Chris Mark[4], Buhari

4   Ardo[1], Kevin. G. Taylor[1], Nico Bigaroni[1], Michael. Pointon[3], Lewis Hughes[1], John Waters[1],

5   Lee Paul[1]

6   1. Department of Earth and Environmental Sciences, Williamson Building, University of
7   Manchester, Manchester, United Kingdom
8   2. Institute of Marine Sciences (CNR-ISMAR), Bologna, Italy
9   3. CASP, Cambridge, United Kingdom
10   4. Department of Geology, Swedish Museum of Natural History, Stockholm, Sweden

11   *Corresponding author e-mail address: natalie.farrell@manchester.ac.uk. Co-author email
12   addresses: li-ning.yang@outlook.com, michael.flowerdew@casp.org.uk, chris.mark@nrm.se,
13   buhari.ardo@gmail.com, kevin.taylor@manchester.ac.uk, nico.bigaroni@manchester.ac.uk,
14   michael.pointon@casp.org.uk, lewis.hughes@manchester.ac.uk,
15   john.waters@manchester.ac.uk, lee.s.paul@manchester.ac.uk,

16   Keywords: Feldspar, CCS, Sandstone, reaction texture, dissolution, precipitation, calcite
17   cement

18   **Abstract**

19   Understanding how the minerals in reservoir rocks respond to CO_2 injection is vital for the
20   success and safety of Carbon Capture and Storage (CCS) projects. Feldspars are the most
21   common mineral in the Earth's crust and act as primary framework grains in sandstones.
22   Compared to quartz, feldspars are mechanically weak and chemically reactive. Dissolved
23   feldspars can re-precipitate as clays, which in CCS reservoirs could impact fluid-flow. While
24   caprock mineral stability is well studied, reservoir mineral reactivity, particularly of feldspars,
25   remains understudied. To address this knowledge gap, we present microstructural and
26   geochemical data from batch experiments that reacted CO_2-enriched fluids with feldspar-
27   bearing sandstone sampled from the Captain Sandstone Member, the primary reservoir for the
28   Acorn CCS Project (UK).

29   Experiments were conducted in a hydrostatic pressure vessel at 70 MPa confining pressure, 50
30   MPa pore pressure, and temperatures ranging from 80°C to 550°C, using CO_2-enriched water
31   to simulate reservoir conditions. Pre- and post-reaction samples were analysed using XRD,

32   SEM-EDS, and XCT to assess microstructural and mineralogical changes. Results show that

33   CO_2:feldspar interactions differ significantly from control experiments involving water alone.

34   At reservoir-relevant temperatures (80°C), incongruent dissolution of K-feldspar weakened

35   grains which led to microfracturing. At 250°C, CO_2 fluids caused total dissolution of calcite

36   grains and cement and selective leaching of calcium from oligoclase, enriching the pore fluid

37   with Ca^{2+}. Above 400°C, coupled dissolution–precipitation processes were observed, including

38   congruent K-feldspar dissolution, secondary porosity development, and localised precipitation

39   of Ca-aluminosilicates and K-bearing phases around dissolving K-feldspars. These

40   transformations could alter reservoir flow pathways and induce mechanical risks, i.e.

41   destabilising nearby faults or initiating reservoir collapse. Given feldspars' prevalence in

42   crustal rocks and CCS sandstone reservoirs, their reactive behaviour under in-situ conditions

43   and in the presence of aggressive fluids demands greater attention.

1. Introduction

45   Carbon Capture and Storage (CCS) projects aim to moderate the impacts of climate changes

46   by injecting supercritical CO_2 into porous rock, such as deep saline aquifers and depleted

47   hydrocarbon sandstone reservoirs, where it is intended to be stored for 10,000

48   years/indefinitely (IPCC, 2005). The productivity and safety of CCS projects hinge on our

49   ability to efficiently flow CO_2 fluids into subsurface rock formations while preventing leakage.

50   A key challenge for success is the ability to predict dynamically changing fluid-flow during

51   injection and CO_2 plume migration (Juanes et al, 2006; Benson and Cole, 2008; Ringrose,

52   2020). This requires both a specific knowledge of the pre-injection micro-scale reservoir

53   properties, e.g., pore volume, pore connectivity, grain texture, and a broader empirical

54   understanding of how injected fluids might mechanically and/or chemically alter this

55   microstructure and thereby impact CCS project efficiency and safety (Rochelle et al, 2004;

56   Hall et al, 2015; Rathnaweera et al, 2015; Shogenov et al, 2015; Fuchs et al, 2019; Foroutan et

57   al, 2021). Experimental studies have explored these CO_2-fluid-sandstone interactions showing

58   that the acidic brines created by dissolution of CO_2 into formation fluids enhances dissolution

59   of carbonate minerals, primarily as cements in sandstone reservoirs (Ross et al, 1982; Bertier

60   et al, 2006; Hangx et al, 2013) with fewer studies reporting CO_2 fluid alteration of reactive

61   aluminosilicates, including feldspars (Bertier et al, 2006; Hall et al, 2015; Lu et al. 2013).

62   Geochemical models indicate that feldspar alteration may result in precipitation of carbonate

63   minerals e.g., dolomite and dawsonite, which could permanently 'lock-in' CO_2 (Durst et al.,

64   2000, Seisenbayev et al, 2023). Feldspar:CO_2 reactivity could substantially influence the

65   performance and stability of CCS reservoirs, yet their response to saturation with CO_2-enriched

66   fluids under reservoir conditions (temperature *and* stress), including reaction types and rates

67   and the consequences of reactivity, is poorly understood (Lu et al. 2013). This is a key

68   knowledge gap especially in polymineralic rocks like sandstone where coupled chemical–

69   mechanical processes are already poorly constrained.

70   *1.1. Feldspar solubility*

71   Feldspars are a volumetrically significant, mechanically weak and chemically reactive

72   framework mineral in sandstones (Tullis and Yund, 1977) and most crustal rocks. In

73   comparison to quartz, feldspars are highly reactive (Knauss and Wolery, 1986; Dove and

74   Crerar, 1990). They can dissolve creating significant secondary porosity (Farrell and Healy,

75   2017) and re-precipitate as clays, which impede fluid-flow and mechanically weaken rocks

76   (Farrell et al, 2021; Summers and Byerlee, 1977; Collettini et al, 2019 respectively), outcomes

77   that could compromise both CCS reservoir efficiency and mechanical integrity. Feldspar

78   solubility is strongly influenced by pH, as demonstrated in early experimental studies (Correns,

79   1961; Wollast, 1967). These investigations established that feldspar dissolution rates increase

80   significantly under acidic conditions due to enhanced hydrolysis of Si–O and Al–O bonds in

81   the crystal lattice, the rate of which is determined by grain surface area (Helgeson et al, 1984).

82   Feldspars are mineralogically well defined, but their subsurface behaviour is uncertain. As key

83   framework minerals in many of Earth's oldest crustal rocks e.g., gneisses, granites and

84   sandstones, they can preserve evidence of their extensive geological histories (e.g. weathering,

85   transport, burial, fluid interaction), which are reflected in their diverse microstructural textures

86   and chemical heterogeneity. This inherited heterogeneity directly affects their reactivity.

87   Across kilometre-scale reservoirs, their solubility can differ significantly based on provenance

88   (detrital sources) and their burial or fluid-flow history (Glasmann, 1992), making some grains

89   more or less prone to dissolution. Chemical alteration has been shown to enhance stress-

90   corrosion cracking in quartz (Scholz, 1972), hence deformation of more reactive feldspars (via

91   chemical dissolution and mechanical cracking) in the presence of chemically active CO_2 fluids

92   is expected.

93   *1.2. Predicting feldspar reaction rates*

94   Mineral reaction rates are typically defined by experiments on powdered rock samples

95   (Brantley et al, 2008). While using powders allows for control over reactant surface area, this

96   method fails to account for the grain-to-grain stresses present in subsurface rocks. Even in

97   hydrostatic experiments, such stresses at the grain scale can significantly accelerate mineral

98   dissolution rates, often exceeding predictions based on powder-derived rate laws (Rutter, 1976;

99   Wheeler, 1991). Considering the inherent weakness of feldspars under pressure-temperature

100   conditions in the shallow crust, these stresses could induce microfracturing, which increases

101   surface area and exposes fresh reactive surfaces that drive further reaction. Geochemical

102   simulations frequently oversimplify feldspars, disregarding their diverse chemical

103   compositions and variable textures i.e., surface areas, which are crucial for accurate reaction

104   rate predictions (Helgeson et al, 1984). Enhanced understanding of feldspars, from quantifying

105   the compositional variability in target reservoirs, to empirical evidence of feldspar:CO_2

106   reactions i.e., dissolution rates and secondary mineral formation, should improve the accuracy

107   of geochemical and reactive transport models. We hypothesise that injection of CO_2 enriched

108   fluids will impact the solubility of *stressed* feldspar grains and potentially alter the properties

109   of sandstone CCS reservoirs, specifically the pore volume, pore connectivity, permeability and

110   geomechanical stability.

111   This paper presents microstructural insights from a suite of coupled chemical:mechanical

112   reaction experiments on feldspar-bearing sandstones from the Early Cretaceous Captain

113   Sandstone Member from the Moray Firth, Scotland, the target reservoir for the Acorn CCS

114   Project (Alcalde et al, 2019), highlighting the impact of CO_2 fluid saturation on reactive

115   framework grains under subsurface conditions. In this study we used an externally heated,

116   hydrostatic pressure vessel to investigate the solubility of various feldspars in a CO_2 saturated

117   sandstone under hydrostatic stress, simulating CCS reservoir conditions in closed batch system

118   experiments. Experiments were conducted at a range of increasing temperatures, effectively

119   accelerating reaction rates simulating mineral reactions over hundreds of years – aligning with

120   the timescales required for CO_2 storage. The temperature dependence of mineral dissolution

121   follows an Arrhenius relationship, linking the reaction rate constant to temperature. For K-

122   feldspar, the baseline rate constant is well-established, and we approximate its temperature

123   dependency using established rate laws for dissolution in varying pH fluids (Helgeson, 1984;

124   Blum and Stillings, 1995). Unlike previous Captain Sandstone experimental studies that

125   focused solely on reservoir mechanical stability using water as a pore fluid at ambient

126   temperatures (Allen et al, 2020) or on the mechanical impact of CO_2 fluids on carbonate cement

127   dissolution at low temperatures in an open pore fluid system (Hangx, 2013), this research

128   explores the role of CO_2 fluid chemistry on the dissolution and stress-induced deformation of

129   arguably more important *framework* grains over geological timescales. These results address a

130   major knowledge gap in CCS reservoir appraisal and have scope to provide empirical

131   constraints for long-term CO_2 containment predictions.

2. Material and Methods

133   This study used an overlapping programme of experimental rock deformation, microstructural

134   and geochemical analysis to characterise the range/integrity of feldspars contained in a CCS

135   target sandstone samples in the context of the reservoir geological history; experimentally

136   assess how feldspars interact with CO_2-enriched fluids under subsurface conditions

137   (temperature, pressure and grain scale stress) and consider the effect of feldspar dissolution

138   and subsequent precipitation of clay minerals on reservoir properties of fluid-flow and

139   mechanical strength. The characterisation of pre-experiment, in situ Captain Sandstone

140   feldspars is summarised in Section 2.1 and fully reported along with a compositional analysis

141   and a provenance model for direct and recycled feldspars in an accompanying paper

142   (Flowerdew et al., in prep).

2.1. Material

144   Sandstones used in these experiments were sampled from a historic petroleum well (14/29a-5,

145   Goldeneye Field, around 8500 ft) and form the target 'D sand' sandstone unit of the planned

146   CO_2 storage reservoir of the Acorn CO_2 storage site, Scotland (Alcalde et al, 2019). The

147   principal reservoir consists of fine to medium grained, high porosity, subarkosic turbidite

148   deposits (Pinnock et al, 2003; Stewart and Marshall, 2020). Detrital mineralogy is dominated

149   by quartz, plagioclase (albite and oligoclase) and orthoclase with some mica, glauconite and

150   mudclasts. Some feldspars in the 'D sand' subdivision of the Member have already been very

151   reactive as shown by secondary porosity (Stewart and Marshall, 2020), more prominent at its

152   top.

153   Captain Sandstone 'D sand' samples comprise poorly cemented subarkose (Folk et al, 1970).

154   Thin section analysis showed that grains are moderately to poorly sorted, 50 to >1000 μm in

155   diameter and loosely packed with around 30% pore area. Intergranular pores are large and

156   irregular or smaller and angular formed by the intersections of multiple rounded grains (Fig

157   1.a). X-ray diffraction analysis showed that samples broadly contain 76% quartz, 8%

158   plagioclase, 8% K-feldspar, 6% clays, predominantly kaolinite plus minor amounts of 1%

159   calcite, 1% glauconite (XRD method and results, Supp. Mat., Table S1). Mineralogical makeup

160   was also determined by using elemental data from an Energy Dispersive X-ray Spectroscopy

161   (EDS) map overlain on a Back-scattered Electron (BSE) map (Fig 1.b).
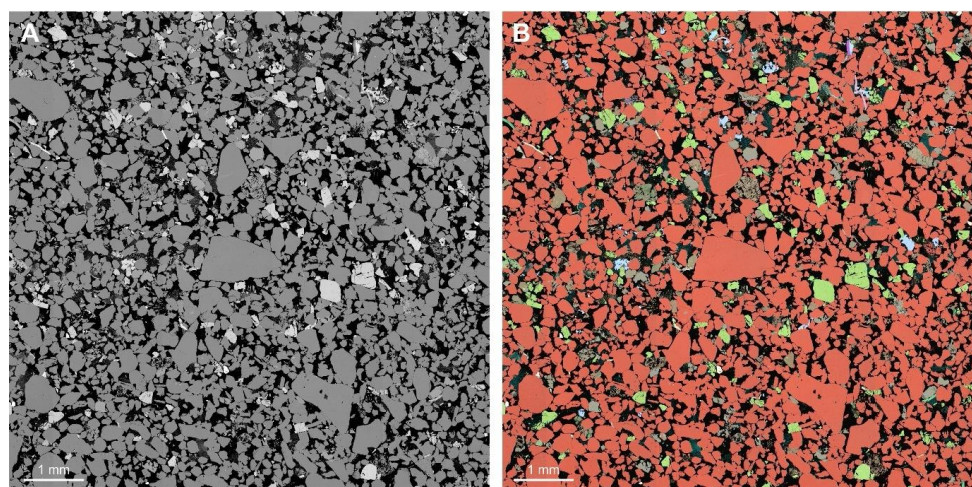
Fig 1. BSE and semi-transparent EDS elemental maps of pre-experiment D sand, Captain Sandstone (a and b respectively). Black = pore/void space, red/orange = quartz, green/yellow = orthoclase feldspar, grey/brown = oligoclase, pale blue = calcite

166   Captain Sandstone feldspars are mineralogically and texturally diverse showing three dominant

167   mineralogies; two plagioclases, intermediate NaCa bearing oligoclase and end member Na-rich

168   albite and K-feldspar (Figure 2.a - e). The reactivity of plagioclase is already apparent in the

169   pre-experiment samples, as indicated by the skeletal texture of albite grains (Fig. 2.b). This

170   texture likely results from the albitisation of oligoclase, driven by chemical exchange where

171   Ca in oligoclase is replaced by Na from brines, substituting Ca^{2+} ions with Na^+, and releasing

172   Ca^{2+} into the fluid (Fig. 2.c). Additionally, plagioclase reaction and dissolution (whether

173   oligoclase or albite) has likely released Al and Si to form kaolinite precipitates during

174   geological diagenesis (Figs. 2.b and c). Both plagioclase and oligoclase grains commonly range

175   between ~100 – 200 µm diameters and display blocky, sub-rectangular grain boundaries with

176   rounded edges (Supp. Mat, Fig. S3). K-feldspars tend to be larger than plagioclases, averaging

177   200-300 µm diameter and display coherent, rounded grain boundaries abutting similarly shaped

178   quartz grains (Fig 2.c). Many K-feldspars show perthite textures with darker fine bands and

179   streaks of albite lamellae oriented along cleavage planes (Fig 2.d and Supp. Mat., Fig S3).

180   Some K-feldspars show reaction in perthite grains with some preferential dissolution of albite

181   lamellae and opening up of intergranular porosity along these features (Fig. 2.f).
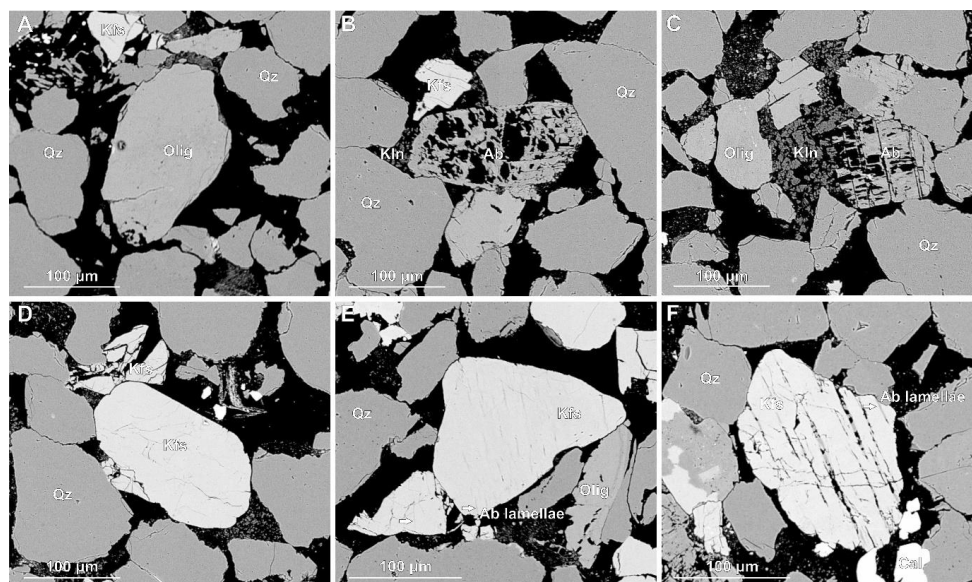
Figure 2. BSE images showing feldspar types including plagioclases, oligoclase (a and c) and albite (b and c) and K- feldspar (c-e) in pre-experiment samples of Captain Sandstone. Abbreviations follow Whitney and Evans, 2010. Quartz (Qz), (Oligoclase (Olig), K-feldspar (Kfs), Albite (Ab), Kaolinite (Kln).

2.2. Experimental method

Eight reaction experiments were performed on 9.5 mm diameter core plugs of Captain Sandstone Member 'D sand' using hydrostatic pressure vessels at ~70 MPa confining pressure (Pc) aka ~3 km burial depth with 50 MPa pore fluid pressure (Pf). Four experiments used CO_2 saturated water as a pore fluid (as a proxy for CO_2 injection), while four control experiments used H_2O under the same conditions. We experimentally modelled the progression of feldspar reactivity under subsurface conditions by conducting experiments across a range of temperatures (from 80°C, aka reservoir conditions, up to 550°C), using elevated temperatures as a proxy for longer reaction time. This approach uses the Arrhenius equation, which describes the temperature dependence of reaction rates, allowing higher temperatures to accelerate mineral reactions and simulate longer-term geochemical processes within practical and repeatable laboratory timescales (calculated reaction rate ratios for these experiments detailed in Supp. Mat., Section S1.1). These results can then be extrapolated to reservoir temperatures following standard practice in mineral-reaction studies (Blum and Stillings, 1995), a methodology commonly used to model reservoir evolution over geological timescales (Brantley et al, 2008; Hangx and Spiers, 2009; Hellmann et al., 2012). Experimental conditions are detailed in Table 1.

Sample ID	Rig ID	Pore Fluid Chemistry	Temperature (°C)	Confining Pressure (MPa)	Pore Fluid Pressure (MPa)	Duration (days)
Dt02	Nimonic 3	H_2CO_3	80	70	50	6
Dm07	Nimonic 2	H_2O	80	70	50	6
Dt01	Nimonic 3	H_2CO_3	250	70	50	10
Dm04	Nimonic 2	H_2O	250	77	50	10
Dt03	Nimonic 3	H_2CO_3	400	70	50	6
Dm06	Nimonic 2	H_2O	400	75	50	6
Dm01	Nimonic 3	H_2O	550	72	50	6
Dm05	Nimonic 3	H_2CO_3	550	80	50	6

Table 1. Experimental conditions for batch reactor tests conducted in triaxial deformation rigs 'Nimonic 2' and 'Nimonic 3'. Core plugs of Captain Sandstone were reacted with differing pore fluid chemistries under constant Pf, Pc and temperatures for durations of 6-10 days with the objective of assessing the influence of pore fluid chemistry and temperature on mineral stability and microstructure.

Experiments were conducted using externally heated triaxial deformation apparatus, 'Nimonic 2' and 'Nimonic 3'. The pressure vessel and sample assembly in these rigs are constructed from nickel alloy (Nimonic® 115) which is highly resistance to oxidation and compatible with carbonic acid and other corrosive fluids at elevated temperatures, preventing piston reactions that could contaminate the rock sample (Fig 3). Samples were contained within annealed copper jackets to isolate them from the water confining fluid, which was pressurised to reservoir conditions using a compressed air pump. Both Pc and Pf were gradually increased in succession up to the required experiment conditions to prevent pore collapse and preserve the starting material grains and microstructure. For control experiments, the pore fluid was tap water (very soft with total hardness of 16 mg/L, Supp. Mat, Table S1), while for CO_2 proxy experiments, the same water was saturated with CO_2 using a SodaStream®. The resulting 'fizzy water' contained ~6 g/L CO_2, yielding a pH of 4. Pf was controlled using a pore volumometer with a piston driven by a DC servo-motor. This system allowed precise adjustments of the piston in and out of a 3 cm³ pressure vessel to maintain a constant Pf through feedback control from a pore pressure transducer. A 50 MPa Pf was used in all experiments to ensure that water remained in a liquid state even above its critical point ~400°C, thereby preserving consistent stress conditions throughout the experiments. Once at pressure, the experiment temperature was applied using upper and lower external furnaces which create a thermal gradient which can be used to position a 'hot spot' within the pressure vessel focused around the relatively small sample. The furnace temperature was increased to the required level using variacs, which control the voltage to the furnaces for precise adjustments. The temperature was then maintained at the set value for six days with stable power regulation from the variacs. Sample temperature was monitored using an inconel-sheathed thermocouple inserted down the upper

231   piston. Pre experiment calibrations showed a temperature range of <2°C along the sample

232   length at 500°C. Experiments were ended by decreasing temperature back to ambient

233   conditions then unloading the Pf and Pc in tandem and in reverse to protect the pore space.
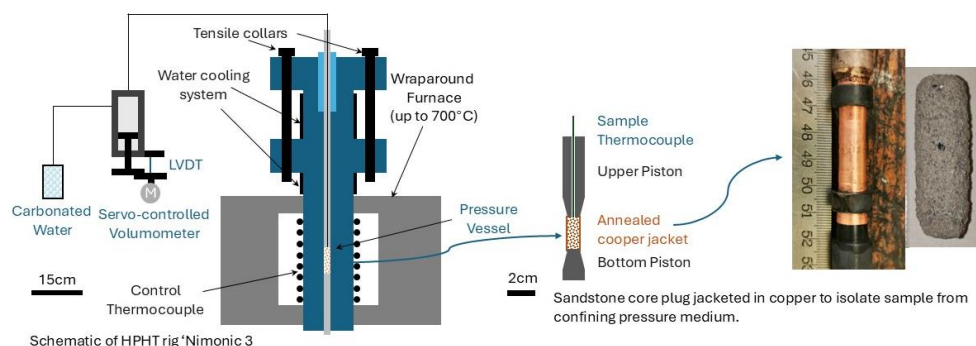

234
235   **Figure 3. Schematic cross section diagram of high pressure, high temperature triaxial rig 'Nimonic 3'**
236   **illustrating the sample assembly within the Nimonic pistons (rhs), confinement of sample with the pressure**
237   **vessel and furnace (centre) and pore volumometer controlling injection and pressure of pore fluid along**
238   **the top piston (lhs).**
239

240   *2.3. Microstructural analysis*

241   Post experiment jacketed core plugs were injected with epoxy under a vacuum and then halved

242   to make thin sections covering the central portion of the sample cylinder. Polished sections

243   were carbon coated before being imaged using a Zeiss Evo MA 15 scanning electron

244   microscope housed at CASP. Back scattered electron (BSE) images and elemental maps were

245   collected using one or a combination of a Zeiss Back Scatter Electron (BSE) detector, an

246   Oxford Instruments Ultim Max 100 Energy dispersive x-ray spectrometer (EDS) detector and

247   an Oxford Instruments Unity detector. Montages of images that cover the thin section were

248   collected at 20 kV and 2000 pA i-probe, and 10 kV and 200 pA i-probe where greater definition

249   imagery was required. Images and data were collected, manipulated and exported using Oxford

250   Instruments AZtec software version 6.1, coupled with the AutoPhaseMap and AZtecFeature

251   analysis and CASP's in-house mineral classification scheme.

252   Microstructural analysis was conducted on BSE and EDS images of pre- and post-experiment

253   thin sections to examine and characterise mineral phases and textures and analyse reaction

254   pathways between grains. This analysis was facilitated by the generation of EDS x-ray spectra

255   for specific points or regions on the map. Post experimental mineral dissolution an/or

256   precipitation was quantified from BSE maps overlain with semi-transparent EDS maps by

257   thresholding the area covered by key mineral phases (K-feldspar, plagioclase, calcite) using

258 image analysis software ImageJ and defining this result as a percentage of the total grain

259 content (see Supp. Mat, for more information). Individual montage images were analysed

260 separately to investigate the heterogeneity of pore and grain distributions (as per method in

261 Farrell and Healy, 2017). Additional 3D micro-CT images were produced of pre and post

262 experiment samples to assess grain deformation and pore networks.

263 **3. Results**

264 Microstructural and compositional changes were identified in all experimentally reacted

265 samples indicating cation exchange between pore fluid and sandstone samples after

266 experimental run times of six days. The experimental duration, stress conditions and pore fluid

267 compositions are summarised in Table 1. In this section we present petrographic results for

268 specific mineral phases and their alteration in the presence of CO_2-enriched water compared

269 with H_2O (i.e. tapwater) (Fig 4-10). Image analysis was used to quantify the extent of mineral

270 alteration in post-experiment samples compared to pre-experiment. Mineral quantifications are

271 presented as box plots to show changes in mean mineral content which could be used in

272 geochemical models and to illustrate the statistical distribution and variability of mineral grains

273 within samples, highlighting dissolution heterogeneity (Fig 11). Additional microstructural

274 data from all experiments are shared in a Supplementary Materials document (Supp. Mat.).

275 *3.1. Alteration of K-feldspar*

276 *3.1.1. K-feldspar:CO_2 enriched pore fluids*

277 Post-experiment BSE imaging reveals significant microstructural changes in K-feldspar grains

278 reacted at different temperatures. Compared to pre-experiment samples, which exhibit minimal

279 fracturing (Fig. 3.c, and Supp. Mat. Fig. S3), post-experiment K-feldspar grains display

280 dissolution, systematic microfracturing and grain fragmentation and development of secondary

281 porosity providing evidence of active mineral alteration during experiments (Fig. 4; Supp. Mat.

282 Figs. S5–S8).

283 At 80°C, open pores develop on grain surfaces as linear and parallel 'cracks' or 'seams' that

284 propagate into grain interiors at high angles, often forming bimodal cross-cutting sets aligned

285 with cleavage planes (Fig. 4.a–b; Supp. Mat. Figs. S5–6) and commonly oriented with albitised

286 lamellae (Fig. 5.a). Some tightly packed K-feldspars are fractured against adjacent grains and

287 crushed between quartz grains, which remain largely intact, suggesting mechanical weakening

288 of stressed K-feldspars, likely enhanced by localised dissolution and development of porous

289   'seams' on the grain edges (Supp. Mat. Fig. S5). At 250°C intergranular dissolution becomes
290   more pronounced, suggesting that increased intergranular fracture density both enhanced
291   reactive surface area and created conduits for further fluid-rock interaction (Fig. 4.c). At 400°C,
292   K-feldspar dissolution is accompanied by the formation of thin (~3 µm), discontinuous calcic
293   aluminosilicate overgrowths along open grain boundaries, particularly around smaller K-
294   feldspar fragments (Fig. 4.d; Fig. 5.b). EDS spot analysis shows overgrowths are chemically
295   equivalent to calcic plagioclase (andesine- anorthite) (Supp Mat. Fig S17). At 550°C,
296   intergranular fractures widen (5–10 µm vs. <5 µm at 400°C), and K-feldspars are segmented
297   by cross-cutting fractures into fragments with rounded, dissolution-modified edges (Fig. 4.e–
298   f). In this sample secondary porosity is widespread and these pores can often be identified by
299   "ghosts" of former grain outlines defined by secondary clay precipitates (Supp. Mat. Figs. S6–
300   S8 and XCT images and animations, https://doi.org/10.6084/m9.figshare.30061294.v1).

301
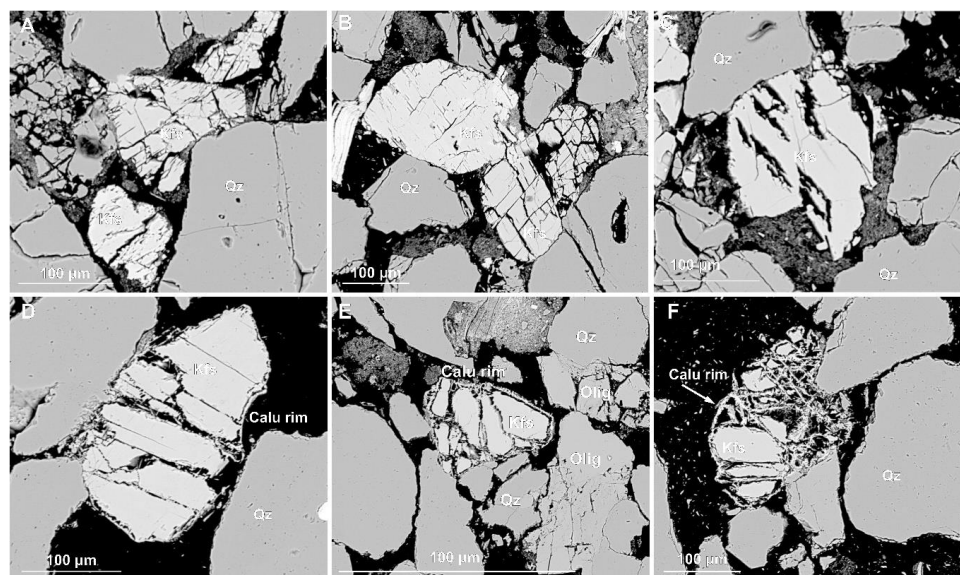
Figure 4. Back scattered electron (BSE) images showing progressive K-feldspar (Kfs) alteration via chemical and mechanical deformation with increasing temperature reaction experiments conducted with CO_2 fluids at hydrostatic conditions, including – dissolution and grain microfracturing at experiments conducted at 80°C (a and b), grain dissolution at 250°C (c), and secondary mineral growth around K-feldspar grains at 550°C (d - f). Quartz (Qz), (Oligoclase (Olig), K-feldspar (Kfs), Calcic aluminosilicate (Calu).

308   Secondary precipitation phases are most prominent at higher temperatures (400–550 °C),
309   appearing as a Ca-rich pale blue and K-rich bright green phases in combined EDS-BSE images
310   (Fig. 5). Precipitates are often located around 'free' edges of grains i.e. not in contact with
311   adjacent grains and become thicker (~10 µm) and more continuous at 550°C, while grain to

312　grain boundaries display concave-convex contacts with adjacent quartz grains, implying
313　differential dissolution and possible influence of intragranular stress on reactivity (Fig. 5.c).
314　Dissolved K-feldspar grain edges typically exhibit irregular, serrated morphologies (Fig. 5.d;
315　Supp. Mat. Figs. S7–S8). In some images, a narrow void separates receding K-feldspar grain
316　edges from calcitic overgrowths, marking a zone where dissolution likely outpaced
317　precipitation (Fig. 4.d–f; Fig. 5.c–d). High-magnification imaging shows outward nucleation
318　of these calcic aluminosilicates at high angles from K-feldspar surfaces and aligned
319　crystallographically with the host grain (Fig. 5.d). Thin K-feldspar strands remain linked to the
320　overgrowths, suggesting ongoing elemental exchange. A K-rich phase, likely mica, is also
321　observed as a bright green band within and beyond the pale blue rims, forming spindly, fibrous
322　morphologies (Fig. 5.d). In the high temperature experiments, the K-rich phase is also
323　precipitated in pore space and pore throats, within the clay masses small crystals of the calcic
324　aluminosilicate has nucleated (Fig. 5.b).
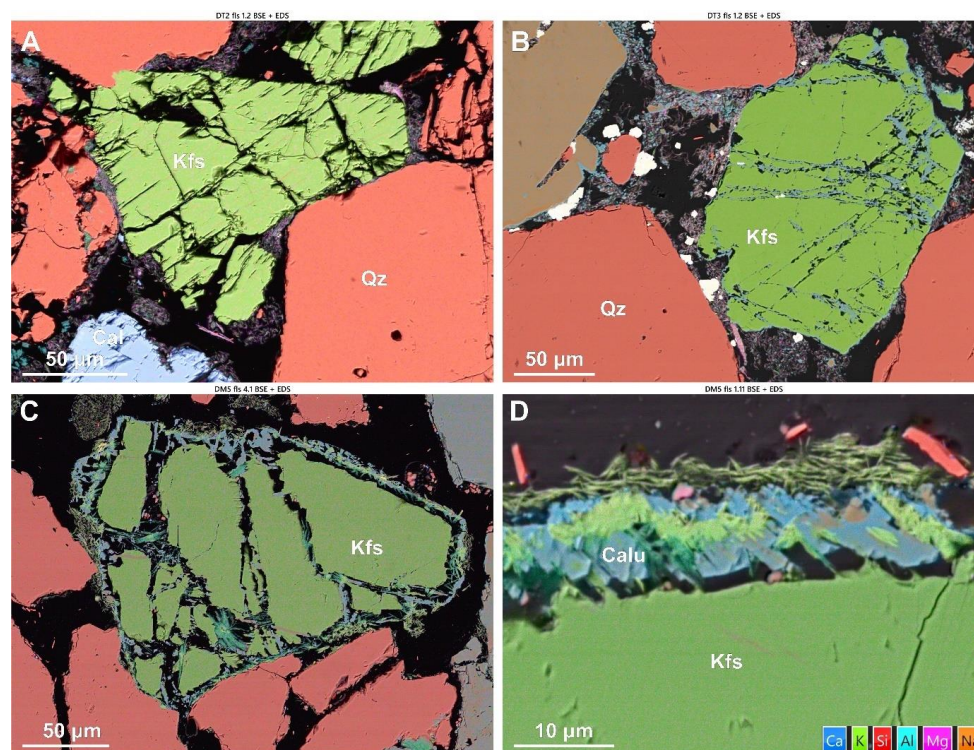
325
326　**Figure 5. High-magnification backscattered electron (BSE) images, overlaid with semi-transparent**
327　**elemental EDS maps, showing progressively enhanced microfracturing, dissolution, and secondary**
328　**precipitation in K-feldspar saturated with CO2 enriched fluids at a range of experimental temperatures**
329　**(80°C (a), 400°C (b), and 550°C (c, d).**

3.1.2. K-feldspar:H₂O pore fluids

In H2O experiments (tap water as pore fluid), post-reaction samples show temperature-dependent microstructural changes distinct from those observed under CO_2-enriched fluid conditions. At 80°C, microfractures in K-feldspar are primarily grain-bound, with curvilinear to sub-parallel orientations (Fig. 6.c–d), the latter suggesting crystallographic control and possible mechanical weakening. These features differ from the chemically driven dissolution seams, serrated grain edges, and widening of intragranular fractures observed in the CO_2 experiments (Section 3.1.1). At higher temperatures 400°C, K-feldspars appear to have been mechanically weakened with post experiment samples showing enhanced intergranular fracturing, local grain crushing, and some convex–concave grain contacts. At 550°C, K-feldspars in H_2O experiments exhibited irregular intergranular fracturing and precipitation of calcic aluminosilicate overgrowths and a K-rich phase which also formed discontinuous rims around grain edges (Fig. 6; Supp. Mat. Figs. S9–S12). However, unlike the CO_2 experiments, these rims are thinner and more spatially limited, and K-feldspar dissolution features were less pronounced. These contrasts highlight the influence of pore fluid chemistry on K-feldspar enhanced reactivity under CO_2-enriched conditions.
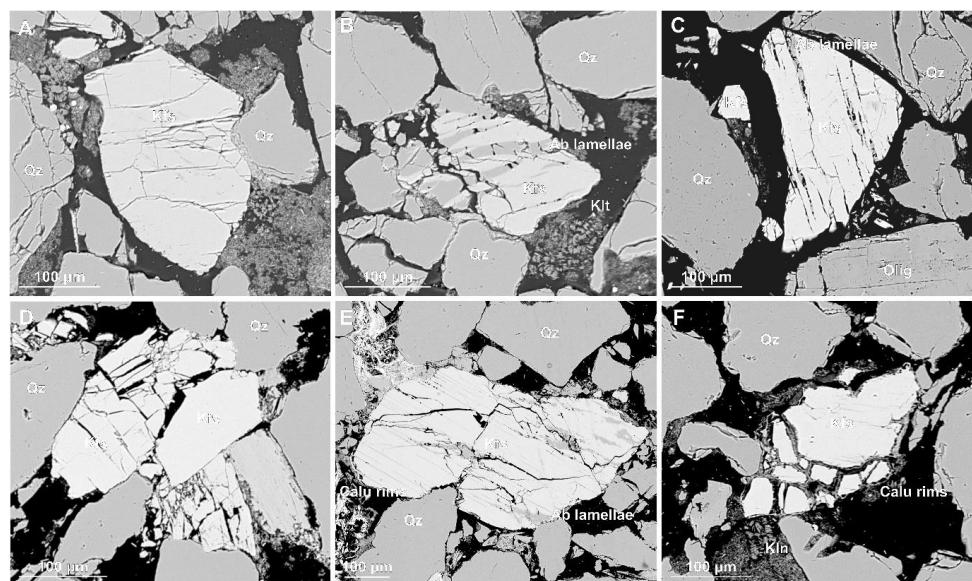
Figure 6. Back scattered electron images showing mechanical fracturing of K-feldspar grains in reaction experiments with H_2O pore fluid at increasing temperatures (80–550°C). Fractures are generally grain bound with irregular, curvilinear traces and some crystallographic alignment at experiments conducted at higher temperatures (c and e) indicating mechanical weakening. Minimal K-feldspar dissolution and persistent presence of albite lamellae suggest reduced alteration under H_2O compared to CO_2-saturated conditions.

3.2. Alteration of plagioclase

3.2.1. Plagioclase:CO_2 enriched pore fluids

The Captain Sandstone Member contains two types of plagioclase: Na-rich end member albite and intermediate oligoclase (Fig 2). The impact of CO_2 enriched pore fluids on oligoclase and albite, is markedly different to each other. At 80°C (reservoir temperature) albite grains remain coherent/intact with their original grain boundaries and skeletal textures (Fig 7.a) while oligoclase grains show minor marginal dissolution or 'scalloping' along grain edges (Fig 7.b). At 250°C, oligoclase grains have complex, indented grain boundaries often surrounded by kaolinite and mixed-element fine clays (Fig. 7.b, c). Some grains show evidence of intergranular pore development or surface etching, though intergranular microfracturing is limited or absent. At higher temperatures (>400°C), intergranular porosity in oligoclase increases due to grain dissolution (Fig. 7.e, f). Albite grains also show significant intergranular porosity, though this appears consistent with the skeletal textures observed in pre-experiment sandstones (Fig. 7.d).
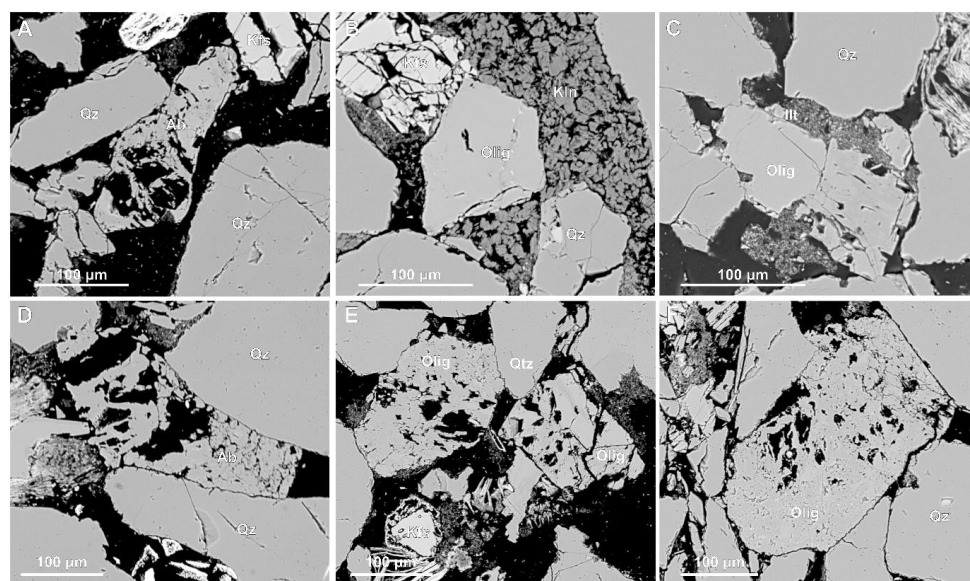
Figure 7. Back scattered electron (BSE) images showing plagioclase grains post reaction experiment condition with CO_2 enriched fluids. Images show no alteration of albite grains at 80°C or 550°C (a and d) while oligoclase grains appear partially dissolved on the grain boundaries at 250°C and 400°C (c) and etching and intergranular porosity at 550°C (e and f).

Combined BSE and EDS images or oligoclase grains reacted at 400°C show leaching of Ca+ from grain edges leaving an original Na-Ca rich grain centre, a ~20-30 μm thick Na rich albitic

374   grain edge plus 2-5 µm calcium aluminosilicate rims similar to features observed on K-feldspar

375   grains but without the void space between the dissolving host grain and secondary precipitate

376   (Fig 8). In contrast, albite shows minimal evidence of chemical interaction with CO_2-enriched

377   fluids at any temperature (Fig. 7.a, d).
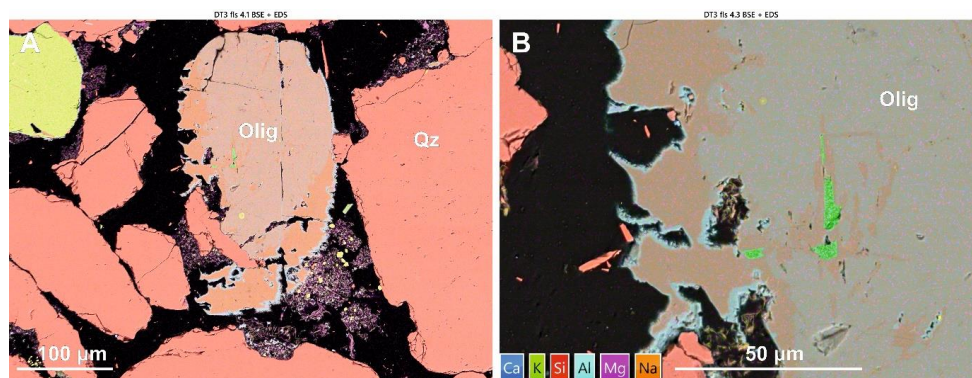
378
379 **Figure 8. Back scattered electron (BSE) images with overlain EDS map showing grain boundary dissolution**
380 **of oligoclase grains reacted with CO_2 fluids at 400°C.**

381   *3.2.2. Plagioclase:H_2O pore fluids*

382   Experiments run with H_2O pore fluids show no obvious chemical alteration of albite or

383   oligoclase at experiments conducted at 400°C and below, but in these samples the oligoclase

384   grains do show more intergranular fractures with many grains fractured along cleavage planes

385   (Fig 9.a). At higher temperatures (550°C) some oligoclase grains show chemical dissolution

386   and 'scalloping' of the grain boundary (Supp. Mat, Fig S12) with few grains exhibit a thick,

387   porous texture calcite overgrowths apparently tracking the original grain boundary as this

388   boundary abuts the contact with quartz grains (Fig 9.e and f). In this sample calcite cements

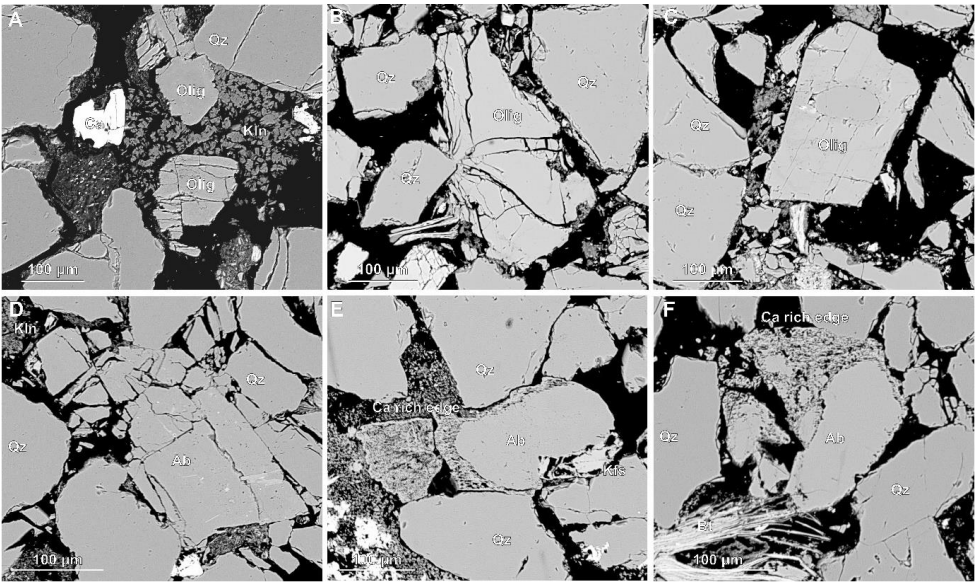389   are still present as singular, isolated patches of cement (Fig 10.c and Supp. Mat, Fig S13).

390

Figure 9. Backscattered electron (BSE) images of plagioclase feldspar grains (including both oligoclase and albite) following reaction with H_2O pore fluid. Images from 80°C and 250°C experiments (a–c) show enhanced mechanical fracturing with minimal evidence of chemical alteration. Albite reacted at 550°C (d) also displays fracturing without signs of chemical dissolution. In contrast oligoclase grains reacted at 550°C appear partially dissolved, with sodium leached from the grains, resulting in a calcite rich grain boundary presenting with a porous 'mesh' texture (e and f).

3.3. Dissolution of calcite grains and cement with CO_2 enriched water and H_2O pore fluids

Pre experiment samples recorded XRD analysis recorded around 1% calcite which occurred as both grains and cement (Supp. Mat, Fig S4). Following the experiments, calcite was nearly entirely removed in the CO_2 experiment samples, whereas it remained visible in post H_2O experiment samples (even at temperatures up to 550 °C) as grains and patches of cement (Figure 10).
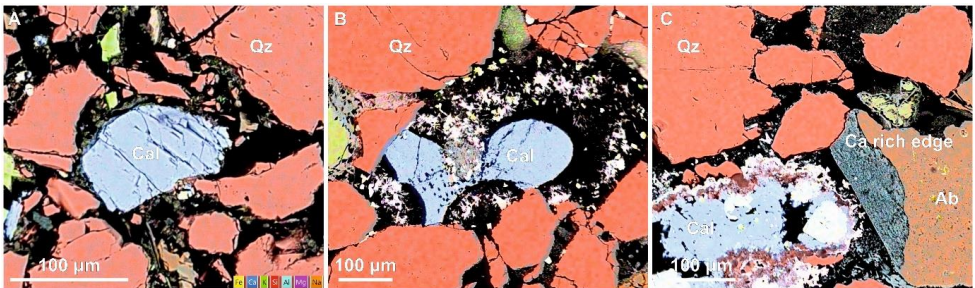

403
404 **Figure 10. Back scattered electron images of calcite grains and calcite cement in post H_2O experiment**
405 **samples reacted at 250°C (a), 400°C (b), 550°C (c).**
406
407

16

408   *3.4. Quantitative microstructural and mineralogical alteration*

409   Image analysis was performed to quantify mineral alteration in both CO_2 and H_2O experiment

410   samples. Specifically, changes in the 2D percentage of pore area and the key reactive minerals

411   (K-feldspar, plagioclase, and calcite) were measured. To account for heterogeneity and spatial

412   distribution, the percentage area of each mineral was quantified from multiple subsections of

413   each thin section (between six and twelve 3x3 mm images per sample) following methodology

414   used in Hall et al (2015). The results are presented using box-and-whisker plots to illustrate the

415   data spread and account for heterogeneity (Fig 11). Two pre-experiment samples, 'Dt' and

416   'Dm', were analysed, each with slightly different pre experiment bulk rock compositions (see

417   Supp. Mat, Table S2). Core plugs from the Dm sample were primarily used in H_2O

418   experiments, while Dt sample core plugs were used in CO_2 experiments.

419   Image analysis revealed minimal changes in 2D pore area between pre-experiment samples,

420   which averaged 29% and 32% pore area and post-experiment reacted with H_2O and CO_2 at

421   80°C and 250°C, which averaged 30% and 32%) (Fig 11.a). However, this decreased to 26%

422   pore area in samples reacted with H_2O at 400°C and 550°C, possibly due to enhanced grain

423   packing and pressure solution observed in images (Fig 9.e and Supp. Mat, Fig S11) and

424   secondary mineral precipitation, while samples exposed to CO_2 at 550°C maintained pore areas

425   over 30% (Fig. 4.a). This difference is likely due to additional secondary porosity produced by

426   K-feldspar and calcite cement and grain dissolution (Supp. Mat, Fig S8) as pressure solution

427   and mineral precipitation are also observed in these samples (Fig 7.f and Supp. Mat, Fig S7).

428   Boxplots show the percentage of reactive grains (K-feldspar, plagioclase, and calcite)

429   expressed as their proportion relative to the total number of mineral grains visible in each image

430   (Fig 11.b – d). The average proportion of K-feldspar grains decreased by nearly half in all

431   samples exposed to H_2O and CO_2, with a more significant reduction observed in post CO_2

432   experiment samples (Fig 11.b). These CO_2 reacted samples also exhibited a more

433   heterogeneous distribution of K-feldspar, as indicated by the wider interquartile ranges on the

434   grey CO_2 box-and-whisker plots compared to the blue H_2O boxes, suggesting variable

435   dissolution across the sample (Fig. 11.b). Due to limitations in image thresholding, albite and

436   oligoclase were grouped together under the category of 'all plagioclase'. In samples reacted

437   with CO_2, the proportion of plagioclase decreased by approximately 25%, indicating some

438   degree of plagioclase dissolution. In contrast, samples reacted with H_2O showed an apparent

439   increase in plagioclase area (Fig. 11.c). This increase likely results from the preferential

440   dissolution of K-feldspar in the H_2O-treated samples, which raises the relative proportion of

441   plagioclase, rather than an actual increase in its absolute abundance. XRD analysis determined

442   ~1% calcite in the pre-experiment samples (Supp. Mat, Table S1), observed in thin sections as

443   carbonate clasts, bioclasts, and carbonate cement patches (Supp. Mat, Fig. S4). Quantitative

444   image analysis revealed a >50% reduction in calcite in CO_2-reacted samples at 80°C and

445   250°C, with almost no calcite at 400°C and 550°C (Fig. 11.d). In contrast, H_2O-reacted samples

446   showed a slight decrease at 80°C, but calcite content remained largely unchanged at higher

447   temperatures.

448
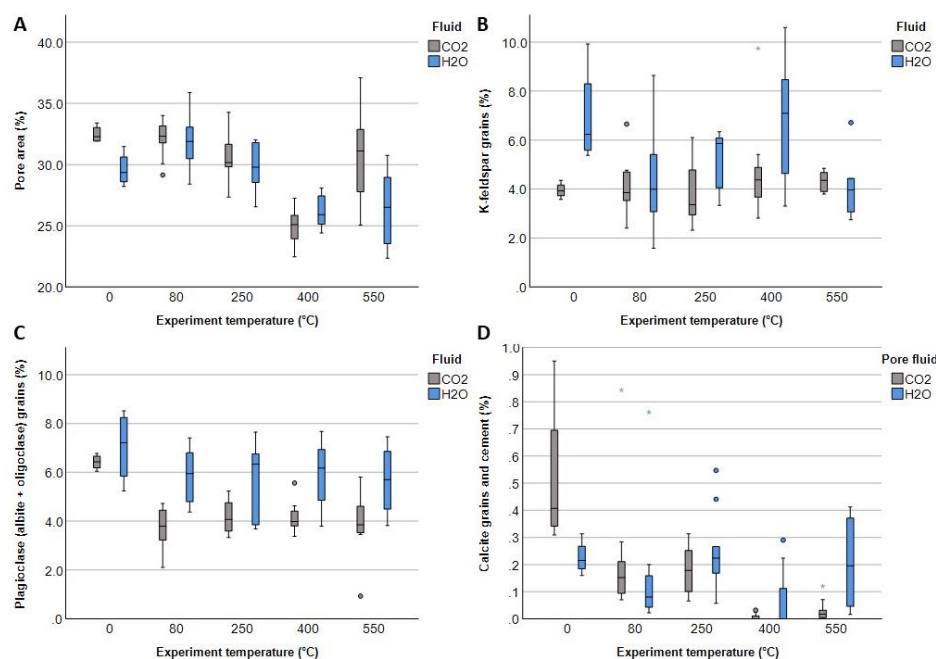
449   **Figure 11. Box and whisker plots showing percentage changes in pore area and reactive mineral content**

450   **in Captain Sandstone samples before and after reaction, experiments, based on thresholded EDS images.**

451   **Two pre-reaction samples, 'Dt' and 'Dm', with slightly different bulk compositions were used: Dm cores**

452   **(H_2O experiments) and Dt cores (CO_2 experiments), shown in grey and blue respectively. Box plots**

453   **display data spread, including median, interquartile range (IQR), and outliers.**

454   **4. Discussion**

455   *4.1. Experimental reaction mechanisms and microstructural evolution*

456   Microstructural analysis of reacted samples reveals a complex interplay of feldspar dissolution

457   and secondary mineral precipitation in the presence of H_2O and CO_2-enriched pore fluids.

458   These reactions are driven by deformation mechanisms such as diffusive mass transfer,
459   including pressure solution, microfracturing, which generates fresh surfaces and increases
460   reactivity, ion exchange and hydrolysis. Key contrasts between H_2O and CO_2 fluid experiments
461   samples include: 1) early incongruent dissolution of K-feldspar in CO_2 experiments conducted
462   at 80 °C, as CO_2-enriched fluids, weakened grains and promoted microfracturing; 2) extensive
463   congruent dissolution K-feldspar in higher temperature >250°C experiments with CO_2, which
464   resulted in grain size reduction, creation of secondary pores and increase in pore area; 3) near-
465   complete dissolution of calcite grains and cements in CO_2 experiments, compared to partial
466   dissolution with H_2O; and 4) partial dissolution and incongruent leaching of calcium from
467   oligoclase grains from 80 °C with CO_2, resulting in grain area reduction that was not observed
468   in H_2O experiments, (Figure 11).

469   *4.1.1. Feldspar deformation and reaction textures*

470   Our results show that at reservoir temperatures CO_2 enriched fluids created a chemically
471   reactive environment that promoted compositionally preferential, incongruent dissolution of
472   K-feldspar and oligoclase. In K-feldspar this produced parallel porous 'seams' that developed
473   on the edge of grains, possibly exploiting cleavage planes (Fig 5.a). These features were absent
474   in higher temperature experiments, possibly because 1) they represented early-stage dissolution
475   textures that were overprinted by later grain dissolution or 2) experiments at higher
476   temperatures (above 250°C) produced a shift in the dominant reaction mechanism from ion
477   exchange reactions (i.e. early incongruent release of K^+, Na^+, and Ca^{2+}) to hydrolysis-driven
478   dissolution (i.e. congruent breakdown of the Si-O framework). Similar temperature-dependent
479   dissolution styles have been observed in previous feldspar reaction experiments on microcline
480   (Fung et al., 1980), albite (Chen et al., 2000), and labradorite (Carroll and Knauss, 2005).

481   K-feldspars with incongruent dissolution textures produced at lower reservoir temperatures
482   appeared to be mechanically weaker and more susceptible to the effects of grain-to-grain
483   stresses under confining pressure, which led to microfracturing and crushing between the more
484   resistant quartz grains (Fig. 4; Supp. Mat. Figs. S5–S7). In turn, these 'fresh' microfractures
485   and fragmented grains created more reactive surfaces, which drove further dissolution in a
486   positive feedback loop of 'incongruent dissolution, stress-induced microfracture, and enhanced
487   grain reactivity'. This process likely accelerated the significant K-feldspar comminution and
488   dissolution textures observed after higher temperature experiments.

489   In plagioclase, interaction with CO_2-enriched fluid had no apparent effect on albite grains but

490   oligoclase showed partial dissolution, evident as wavy grain boundaries and localised

491   compositional zoning (Fig 8). EDS analysis indicated that this texture was formed by

492   incongruent dissolution, with calcium being selectively leached from the edge of grains leaving

493   a sodium rich outer zone around an intact Ca-Na rich grain centre (Fig 8). A thin Ca-rich rim

494   at the grain edge was also observed. While grain weakening evidenced by microfracturing was

495   less evident in altered oligoclase grains, pressure solution features (e.g., concave–convex

496   contacts) suggests stress-driven mass transfer played a role in the evolution of these dissolution

497   textures.

498   *4.1.2. Coupled dissolution-precipitation and ion exchange*

499   At >400°C in both H_2O and CO_2 experiments, K-feldspar dissolution was coupled with

500   secondary mineral precipitation. This included pore-filling masses, overgrowths and fracture

501   fills of calcic aluminosilicate rims and K-bearing clays associated with dissolving K-feldspar

502   grains (Fig 5.d and Supp Mat., Fig S14). Despite the sharp boundary between the primary K-

503   feldspar and secondary calcic aluminosilicates, optical continuity between secondary phases

504   and host grains indicates epitaxial growth via ion exchange as Ca^{2+} in the pore fluid was

505   substituted for K^+ in K-feldspar. Quantitative surface area analysis showed K-feldspar and

506   calcite as dominant dissolving phases in H_2O and CO_2 experiments (Fig 11). While incongruent

507   dissolution of oligoclase in CO2 experiments contributed additional Ca^{2+} via leaching (Fig. 8).

508   The resulting enrichment likely induced supersaturation, triggering precipitation of calcic

509   aluminosilicates and potassic aluminosilicates (K-clays) (Fig 5).

510   Similar coupled dissolution-precipitation (CDP) reactions in K-feldspar have previously been

511   observed both in nature (Cole et al., 2004, Moore et al, 2005; Baines and Worden; 2004) and

512   experiments (Putnis et al., 2007b; Niedermeier et al, 2009; Norberg et al., 2011; Abart et al.,

513   2012). For example, albitisation of sanidine and orthoclase by Na-Cl fluids via CDP produced

514   sharp reaction interfaces with crystallographically aligned albite overgrowths (Norberg et al.,

515   2011). In another experimental study, the replacement of albite by K-feldspar produced sharply

516   defined reaction fronts while preserving the crystallographic orientation of the host grain

517   (Niedermeier et al., 2009). Additionally, similar to the parallel dissolution seams observed in

518   our study, Niedermeier reported aligned 'tubular nanopores' normal to the replacement interface

519   which they interpreted as pathways for fluid access to the reaction front (Niedermeier et al.,

520   2009). Such nanotube formation appears to be a common feature of reaction fronts in mineral

521   lattices (Harlov et al., 2005; Zeitler et al., (2017).

522   *4.1.3. Anorthitisation of K-feldspar comparison to previous studies*

523   In this study, we observed the replacement of K-feldspar by calcic aluminosilicates i.e.
524   'anorthitisation', under experimental conditions (400°C, 70MPa confining pressure).
525   Anorthitisation has been described in natural systems, e.g. the transformation of andesine to
526   anorthite in the presence of Ca^{2+}-rich meteoric fluids (Mora et al., 2009) and has been described
527   conceptually in the framework of CDP reactions (Putnis, 2009). Though K-feldspar alteration
528   via direct K^+- Ca^{2+} substitution has not been described previously in geological settings, there
529   are natural examples of K-feldspar alteration involving Ca-bearing fluids. These include high
530   temperature hydrothermal systems where K-feldspar is replaced by Na-Ca plagioclase and
531   myrmekite textures form via K, Na, and Ca exchange (Chakrabarty et al., 2023). And low
532   temperature settings in CO_2-rich basins like Otway and Bravo Dome where fluid acidification
533   drives feldspar dissolution and precipitation of Ca-bearing phases such as dawsonite and calcic
534   zeolites, (Mora et al., 2009; Wigley et al., 2013; Baines and Worden, 2004).

535   While the replacement of K-feldspar by calcic aluminosilicates via ion exchange has not been
536   previously described under controlled laboratory conditions in geoscience, it has been explored
537   and established in materials science. Specifically, anorthitisation via ion exchange is being
538   investigated as a method for extracting potassium from K-feldspar using calcium-bearing fluids
539   as an alternative method for fertiliser production. Although not yet commercially implemented,
540   laboratory studies have shown K^+ leaching from K-feldspar powders at temperatures as low as
541   65°C (Ma et al., 2016; Ciceri et al., 2017), and the formation of calcic aluminosilicate phases,
542   texturally similar to those observed in our experiments, at 160 °C (Liu et al., 2015; Yuanyuan
543   et al., 2020; Haseli et al., 2020; Zhai et al., 2021). These findings suggest that ion exchange via
544   CDP observed in our study may represent a previously unrecognised mechanism for K-feldspar
545   alteration in the presence of CO_2-enriched fluids.

546   *4.1.4. Source of calcium*

547   In natural systems, Ca^{2+} is typically derived from hydrothermal fluids or CO_2-enriched waters
548   that leach calcium from carbonates, plagioclase, or mafic phases. In our experiments, elevated
549   calcium in the pore fluid resulted from 1) dissolution of calcite grains and cement, prominent
550   in all CO_2 experiments, and to a lesser degree in H_2O experiments >400°C, and 2) partial
551   dissolution of oligoclase, observed only in CO_2 experiments. Incongruent dissolution of
552   plagioclase is well established, for example, a previous experimental study on labradorite
553   showed that calcium release rates exceeded silica release by a factor of three, highlighting

554 strongly incongruent behaviour (Knauss and Wolery, 1988). This likely explains why we

555 observed preferential calcium leaching from oligoclase, producing a Na-rich rim around an

556 intact Na-Ca grain core. The precipitation of secondary calcic aluminosilicate phases may have

557 further contributed to calcium leaching, as the removal of Ca^{2+} from the pore fluid enhanced

558 chemical disequilibrium and promoted continued oligoclase dissolution.

559 Previous studies on the Captain Sandstone 'D sand' also observed calcite dissolution during

560 CO_2 flow-through experiments at <60 °C (Hangx et al., 2013). However, this study focused on

561 the effect of calcite dissolution on rock mechanical strength and, although they also noted K-

562 feldspar dissolution, did not examine the coupled mechanisms driving geochemical alteration

563 or potential for ion exchange.

564 *4.1.5. Role of stress*

565 Although our experiments were successfully designed to limit mechanical compaction

566 (confirmed by maintenance of pore area in H_2O and CO_2 runs up to 250 °C), features indicative

567 of chemical compaction via pressure solution, such as concave–convex grain contacts, were

568 observed in both H_2O and CO_2 experiments above 400 °C. These suggest localised, stress-

569 assisted dissolution at grain contacts under high temperature aka faster reaction rate

570 experiments. This dissolution likely increased local K^+ concentration, providing micro-zones

571 of supersaturation and promoting precipitation in adjacent lower-stress areas around grain

572 boundaries. Analogous features are seen in natural CO_2 reservoirs like the Supai Sandstone

573 Formation, where dawsonite precipitates are spatially associated with corroded K-feldspar and

574 in the Triassic Chaunoy Formation, which associates feldspar dissolution textures with

575 carbonate and zeolite formation (Moore et al., 2005; Baines and Worden, 2004 respectively).

576 *4.2. Comparison to previous studies on CO2:sandstone interaction*

577 The enhanced dissolution of K-feldspar and calcite in CO_2-enriched fluids observed in our

578 study aligns with previous experimental studies. For instance, a three-month CO_2 flow-through

579 experiment at 140 °C resulted in K-feldspar dissolution, grain size reduction, and secondary

580 porosity, leading to a 20% increase in porosity and increased permeability (Hall et al., 2015).

581 Although no secondary precipitation occurred due to constant undersaturation, deformation

582 textures e.g. altered feldspars and secondary porosity, closely resemble observations from our

583 experiments. In addition to the dissolution of calcite cement noted in the Hangx study described

584 above, carbonate mineral dissolution in sandstones reacted with CO2-enriched fluids is

585 experimentally well established. Several studies have shown increased calcium concentrations
586 in pore fluids following saturation of sandstone samples with CO_2-enriched brines, many
587 accompanied by a corresponding permeability increase (Ross et al., 1982; Sayegh et al., 1990;
588 Hall, 2015; Foroutan, 2021). Precipitation of secondary phases was apparently not a limiting
589 factor for K-feldspar dissolution in our experiments, contrasting with the experimental results
590 of Lu et al, (2013), possibly due to fracture-induced increases in feldspar-fluid surface area.

591 Studies on feldspar alteration in geological CO_2-injection projects and natural CO_2 reservoirs
592 also support our findings. In a study on the microstructural impact of CO_2 on sandstone in an
593 engineered subsurface setting, the microstructure of pre- and post-core CO_2 flood sandstones
594 from the Pembina Cardium CO_2 Monitoring Project in Canada showed partial dissolution of
595 K-feldspar grains after two years of CO_2 injection (Nightingale et al., 2009). And as previously
596 noted, natural CO_2 reservoirs such as Bravo Dome also show feldspar alteration and secondary
597 mineral formation linked to long-term CO_2 exposure (Wigley et al., 2012). These findings
598 confirm that feldspar alteration and associated secondary porosity development can occur over
599 relatively short timescales in the subsurface and are comparable in character to the features we
600 have observed in our higher-temperature experimental system.

601 *4.3. Implications for CCS reservoirs*

602 Our findings have several *direct* implications for geological storage of CO_2. Firstly, they
603 demonstrate that K-feldspar and oligoclase in CO_2-enriched fluids at reservoir-relevant
604 conditions can undergo rapid alteration including grain weakening, microcracking, dissolution
605 and the development of secondary porosity. Second, they show that dissolution of even small
606 amounts (e.g. 1%) of calcite grains and cement or leaching of calcium from plagioclase can
607 elevate Ca^{2+} concentrations in the pore fluid and, depending on local fluid composition and
608 saturation states, promote ion exchange with K-feldspar and drive the precipitation of calcic
609 aluminosilicates and K-bearing clays. Third, the presence of pressure solution textures suggests
610 that local stress concentrations create grain-scale chemical disequilibria, enhancing feldspar
611 dissolution and promoting localised mineral precipitation, processes that are often overlooked
612 in geochemical models of CCS systems.

613 These microstructural alterations have important implications for reservoir integrity and CO2
614 project performance. Weakening and dissolution of framework feldspars (~16 % of the D Sand)
615 could reduce compressive strength, alter elastic properties, and modify porosity. These
616 properties are key parameters in both geomechanical and fluid flow models and could alter the

617   predicted reservoir behaviour. Such changes would be especially critical near structural

618   features like faults, where shifts in strength or porosity may alter fault stability during fluid

619   injection/depletion. While the relatively unfaulted Acorn CCS site may be less susceptible to

620   fault reactivation, microstructural changes such as feldspar weakening and dissolution could

621   still lead to mechanical compaction and reservoir fracturing. The impact of this may affect the

622   ability to flow CO2 fluids into the reservoir, i.e. productivity. However, in some cases, such as

623   the Ekofisk field, reservoir collapse and compaction have paradoxically enhanced permeability

624   and improved production (Teufel, 1996).

625   Secondary mineral precipitation, such as K-bearing illite, could reduce permeability and hinder

626   CO2 injection/migration, but feldspar dissolution, especially of Ca-bearing phases like

627   oligoclase may enhance long-term CO2 sequestration by releasing Ca^{2+}. that can become

628   incorporated into secondary phases, possibly even locking in carbon. However, if Ca^{2+} instead

629   bonds with dissolving K-feldspar, it may reduce carbonate formation and limit carbon trapping

630   through mineralisation. Dawsonite did not form in our experiments, likely due to the low Na

631   and Cl content of our fluids. In natural CCS settings, brine compositions with higher Na

632   concentrations could promote dawsonite or other Na-bearing phase formation via K-feldspar

633   replacement. Instead, we observed formation of a calcic aluminosilicate, although we cannot

634   confirm whether it contained carbon, as our carbon-coated thin sections compromised EDS

635   detection.

636   *4.4. Experimental limitations*

637   While our findings offer empirical evidence for feldspar reactivity in CO_2-enriched fluids,

638   several limitations are acknowledged. Most notably, the elevated temperatures used in some

639   experiments accelerated reaction kinetics beyond those typical of natural systems. However,

640   the occurrence of similar dissolution reactions, albeit to a lesser extent, at reservoir

641   temperatures supports the relevance of our results to CCS reservoir and a comparison to

642   reaction rates on a geological timescale has been calculated (Supp Mat, Section S1.1). Post-

643   quench precipitation of secondary phases cannot be ruled out, although the presence of well-

644   crystallised calcic aluminosilicate in optical continuity with host grains strongly suggest that

645   these minerals formed in situ during the experiments. This interpretation is consistent with

646   previous work which noted similar limitations and applied the same criteria to distinguish in-

647   experiment from post experiment precipitation (Rosenqvist et al., 2001).

648 For this study, we employed batch reactor experiments because they allow direct comparison
649 with the geochemical models used in the Acorn CCS Project (Shell, 2015. Batch systems are
650 optimal for studying both dissolution and precipitation processes as they more closely mimic
651 the generally static fluid conditions in subsurface reservoirs than flow through setups.
652 However, batch reactors do not simulate the effects of fluid flow, which in a CCS reservoir
653 would significantly influence reaction kinetics as the dissolved phases would be transported,
654 both reducing supersaturation and making for a dynamic ongoing pore fluid chemistry. As
655 previous CO_2:sandstone flow-through experiments have shown, undersaturation of the fluid
656 suppresses precipitation but enhances feldspar dissolution (Hall et al, 2015). For understanding
657 the interplay between reaction rate and transport in dynamic subsurface environments like CCS
658 reservoirs, both experimental styles are important. Another limitation is the use of tap water
659 rather than brine. Although selected to avoid the overly reactive behaviour of deionised water,
660 our fluid lacks the high Na^+ and Cl^- content typical of formation waters, which may influence
661 both dissolution and secondary mineral precipitation. Future work should incorporate brine
662 compositions and use flow-through systems under triaxial stress to better simulate reservoir
663 conditions.

664 Despite these limitations, our results provide some of the first experimental evidence for CO_2
665 fluid induced K-feldspar alteration under controlled conditions relevant to CCS subsurface
666 settings. This supports the idea that K^+–Ca^{2+} exchange can occur via coupled dissolution–
667 precipitation mechanisms, with implications for feldspar reactivity, reservoir evolution, and
668 long-term mineral trapping in CCS scenarios.

669 **5. Summary**

670 This study offers new insights into mineral transformations and grain-scale weakening in a
671 planned CCS reservoir - processes that have been previously recognised in CO_2:sandstone
672 studies but never systematically investigated. This study also provides the first geological
673 evidence that Ca^{2+} released from experimental dissolution of detrital feldspar grains in a
674 sandstone (i.e. not freshly ground-up powder) can drive in-situ K^+ - Ca^{2+} ion exchange in K-
675 feldspar under realistic subsurface conditions.

676 Consistent with our hypothesis, experimental results showed that:

677 1) K-feldspar is more reactive than expected when exposed to disequilibrium fluids (both H_2O
678 and CO_2) under subsurface hydrostatic stresses at temperature; and

679 2) in comparison to H_2O, CO_2-enriched fluids significantly altered solubility of both

680 plagioclase and K-feldspar and produced distinct microstructural changes even during short (6-

681 day) experiments.

682 At reservoir temperatures (80 °C), CO_2-enriched fluids induced incongruent dissolution and

683 deformation of K-feldspar and dissolution of detrital calcite via ion exchange underscoring the

684 relevance of these transformations to CCS settings. At higher temperatures, where reaction

685 kinetics were accelerated, both H_2O and CO_2 fluids promoted dissolution of reactive minerals

686 - K-feldspar, oligoclase, and calcite - leading to the precipitation of secondary aluminosilicate

687 and clay phases. We propose that these transformations reflect a coupled dissolution–

688 precipitation mechanism, where Ca^{2+} released from calcite and oligoclase dissolution activates

689 and sustains K-feldspar alteration and subsequent dissolution. Crucially, the formation of

690 epitaxial Ca-bearing overgrowths on K-feldspar grains provides clear experimental evidence

691 for K^+ - Ca^{2+} ion exchange. While this anorthitisation of K-feldspar has been engineered in

692 materials science studies using Ca-rich fluids, this study is the first to demonstrate the reaction

693 occurring *in situ*—i.e., within intact rock, under subsurface stress using weakly CO_2-enriched

694 fluids.

695 As discussed, previous experimental and natural studies show that feldspar alteration can

696 involve coupled dissolution, ion exchange, and secondary mineral formation. Our findings

697 build on this by demonstrating more varied modes of feldspar transformation with CO_2-

698 enriched and calcium bearing fluids. While consistent with earlier CO_2- sandstone work, this

699 study uniquely combines microstructural and geochemical changes created under known

700 conditions to map possible reaction pathways and quantify the impact on mineral texture and

701 microstructure. These processes, often difficult to capture in reactive transport models, could

702 significantly affect reservoir properties like pore volume, fluid flow, and geomechanical

703 integrity.

704 *5.1. Outlook on remaining challenges*

705 Chemical mapping and compositional analyses suggest that feldspar zoning may influence

706 dissolution behaviour, although further investigation is required. The original chemical

707 homogeneity of the feldspars and their provenance appear to be important factors controlling

708 reactivity, which could have implications for other arkosic reservoir systems. More broadly,

709 this study raises new questions about the timing and mechanisms of feldspar reactivity in

710 stressed, fluid-saturated environments. It demonstrates the need to reconsider CCS appraisal

approaches, which often assess geochemical and geomechanical behaviour separately. Our
findings support a more integrated understanding of these processes and have wider relevance
for other subsurface applications, including geothermal energy and mineral extraction. Finally,
quantifying feldspar dissolution kinetics remains a key challenge due to the formation of
secondary clays and interactions with other phases. Future work should focus on simplified,
monomineralic synthetic systems with controlled textures and grain sizes to isolate, and thereby
better constrain, reaction rates.

Author contribution: Design of this project and acquisition of funding were carried out by
Natalie Farrell, Michael Flowerdew, and Kevin Taylor. Natalie Farrell designed the
experiments and prepared samples, and PDRA's Lining Yang and Nico Bigaroni carried them
out. Lee Paul provided technical support i.e. tooling, fixing the rig pump. Michael Flowerdew
and Lewis Hughes collected SEM BSE and EDS images. Natalie Farrell, Michael Flowerdew,
Chris Mark and Michael Pointon conducted analysis of microstructural and geochemical data.
Buhari Ardo and Kevin Taylor collected XCT data and processed and analysed the images.
John Waters carried out XRD analysis. Natalie Farrell prepared the manuscript with
contributions from all co-authors.

References

Alcalde, J., Heinemann, N., Mabon, L., Worden, R.H., De Coninck, H., Robertson, H., Maver,
M., Ghanbari, S., Swennenhuis, F., Mann, I. & Walker, T., 2019. *Acorn: Developing full-chain
industrial carbon capture and storage in a resource- and infrastructure-rich hydrocarbon
province*. Journal of Cleaner Production, 233, pp. 963–971.

Baines, S.J. and Worden, R.H., 2004. The long-term fate of CO_2 in the subsurface: natural
analogues for CO_2 storage.

742 Benson, S.M. and Cole, D.R., 2008. CO2 sequestration in deep sedimentary
743 formations. *Elements*, *4*(5), pp.325-331.

744 Bertier, P., Swennen, R., Laenen, B., Lagrou, D. and Dreesen, R., 2006. Experimental
745 identification of CO2–water–rock interactions caused by sequestration of CO2 in Westphalian
746 and Buntsandstein sandstones of the Campine Basin (NE-Belgium). *Journal of geochemical*
747 *exploration*, *89*(1-3), pp.10-14.

748 Blum, A.E., Stilling. L. 1995. Feldspar dissolution kinetics. *Chemical weathering rates of*
749 *silicate minerals*, pp.291-351. Brantley, S.L., Kubicki, J.D. and White, A.F. eds., 2008.
750 Kinetics of water-rock interaction.

751 Carroll, S.A. and Knauss, K.G., 2005. Dependence of labradorite dissolution kinetics on CO2
752 (aq), Al (aq), and temperature. *Chemical Geology*, *217*(3-4), pp.213-225.

753 Putnis, C.V., Geisler, T., Schmid-Beurmann, P., Stephan, T. and Giampaolo, C., 2007. An
754 experimental study of the replacement of leucite by analcime. *American Mineralogist*, *92*(1),
755 pp.19-26.

756 Chakrabarty, A., Mukherjee, S., Karmakar, S., Sanyal, S. and Sengupta, P., 2023. Petrogenesis
757 and in situ U-Pb zircon dates of a suite of granitoid in the northern part of the Central Indian
758 tectonic Zone: Implications for prolonged arc magmatism during the formation of the
759 Columbia supercontinent. *Precambrian Research*, *387*, p.106990.

760 Chen, Y., Brantley, S.L. and Ilton, E.S., 2000. X-ray photoelectron spectroscopic measurement
761 of the temperature dependence of leaching of cations from the albite surface. *Chemical*
762 *Geology*, *163*(1-4), pp.115-128.

763 Ciceri, D., de Oliveira, M. and Allanore, A., 2017. Potassium fertilizer via hydrothermal
764 alteration of K-feldspar ore. *Green Chemistry*, *19*(21), pp.5187-5202.

765 Cole, D.R., Larson, P.B., Riciputi, L.R. and Mora, C.I., 2004. Oxygen isotope zoning profiles
766 in hydrothermally altered feldspars: Estimating the duration of water-rock
767 interaction. *Geology*, *32*(1), pp.29-32.

768 Collettini, C., Tesei, T., Scuderi, M.M., Carpenter, B.M. and Viti, C., 2019. Beyond Byerlee
769 friction, weak faults and implications for slip behavior. *Earth and Planetary Science*
770 *Letters*, *519*, pp.245-263.

771   Correns, C.W., 1961, February. Experiments on the decomposition of silicates and discussion

772   of chemical weathering. In *Clays and Clay Minerals (National Conference on Clays and Clay*

773   *Minerals)* (Vol. 10, pp. 443-459). Cambridge University Press & Assessment.

774   Dove, P.M. and Crerar, D.A., 1990. Kinetics of quartz dissolution in electrolyte solutions using

775   a hydrothermal mixed flow reactor. *Geochimica et cosmochimica acta*, *54*(4), pp.955-969.

776   Durst, P. and Vuataz, F.D., 2000, June. Fluid-rock interactions in hot dry rock reservoirs. A

777   review of the HDR sites and detailed investigations of the Soultz-sous-Forets system.

778   In *Proceedings World Geothermal Congress* (pp. 3677-3682). Kyushu-Tohoku Japan.

779   Farrell, N.J.C. and Healy, D., 2017. Anisotropic pore fabrics in faulted porous

780   sandstones. *Journal of Structural Geology*, *104*, pp.125-141.

781   Farrell, N.J.C., Debenham, N., Wilson, L., Wilson, M.J., Healy, D., King, R.C., Holford, S.P.

782   and Taylor, C.W., 2021. The effect of authigenic clays on fault zone permeability. *Journal of*

783   *Geophysical Research: Solid Earth*, *126*(10), p.e2021JB022615.

784   Folk, R.L., Andrews, P.B. and Lewis, D.W., 1970. Detrital sedimentary rock classification and

785   nomenclature for use in New Zealand. *New Zealand journal of geology and geophysics*, *13*(4),

786   pp.937-968.

787   Foroutan, M., Ghazanfari, E. and Amirlatifi, A., 2021. Variation of failure properties, creep

788   response and ultrasonic velocities of sandstone upon injecting CO_2-enriched

789   brine. *Geomechanics and Geophysics for Geo-Energy and Geo-Resources*, *7*(2), p.27.

790   Fuchs, S.J., Espinoza, D.N., Lopano, C.L., Akono, A.T. and Werth, C.J., 2019. Geochemical

791   and geomechanical alteration of siliciclastic reservoir rock by supercritical CO_2-saturated brine

792   formed during geological carbon sequestration. *International Journal of Greenhouse Gas*

793   *Control*, *88*, pp.251-260.

794   Fung, P.C., Bird, G.W., McIntyre, N.S., Sanipelli, G.G. and Lopata, V.J., 1980. Aspects of

795   feldspar dissolution. *Nuclear technology*, *51*(2), pp.188-196.

796   Glasmann, J.R., 1992. The fate of feldspar in Brent Group reservoirs, North Sea: A regional

797   synthesis of diagenesis in shallow, intermediate, and deep burial environments. *Geological*

798   *Society, London, Special Publications*, *61*(1), pp.329-350.

799   Hall, M.R., Dim, P.E., Bateman, K., Rochelle, C.A. and Rigby, S.P., 2015. Post-CO_2 injection

800   alteration of pore network geometry and intrinsic permeability of Permo Triassic sandstone

801   reservoir". Geofluids, 10.1111/gfl. 12146.

802   Hangx, S., Bakker, E., Bertier, P., Nover, G. and Busch, A., 2015. Chemical–mechanical
803   coupling observed for depleted oil reservoirs subjected to long-term CO2-exposure–A case
804   study of the Werkendam natural CO2 analogue field. *Earth and Planetary Science Letters*, *428*,
805   pp.230-242.

806   Harlov, D.E., Wirth, R. and Förster, H.J., 2005. An experimental study of dissolution–
807   reprecipitation in fluorapatite: fluid infiltration and the formation of monazite. *Contributions*
808   *to Mineralogy and Petrology*, *150*(3), pp.268-286.

809   Haseli, P., Majewski, P., Christo, F., Raven, M., Klose, S. and Bruno, F., 2020. Experimental
810   kinetic analysis of potassium extraction from ultrapotassic syenite using NaCl–CaCl2 salt
811   mixture. *Acs Omega*, *5*(27), pp.16421-16429.

812   Helgeson, H.C., Murphy, W.M. and Aagaard, P., 1984. Thermodynamic and kinetic constraints
813   on reaction rates among minerals and aqueous solutions. II. Rate constants, effective surface
814   area, and the hydrolysis of feldspar. *Geochimica et Cosmochimica Acta*, *48*(12), pp.2405-2432.

815   Hellmann, R., Wirth, R., Daval, D., Barnes, J.P., Penisson, J.M., Tisserand, D., Epicier, T.,
816   Florin, B. and Hervig, R.L., 2012. Unifying natural and laboratory chemical weathering with
817   interfacial dissolution–reprecipitation: a study based on the nanometer-scale chemistry of
818   fluid–silicate interfaces. *Chemical Geology*, *294*, pp.203-216.

819   IPCC, 2005. *Special Report on Carbon Dioxide Capture and Storage*. Cambridge:
820   Cambridge University Press, 431 pp.

821   Juanes, R., Spiteri, E.J., Orr Jr, F.M. and Blunt, M.J., 2006. Impact of relative permeability
822   hysteresis on geological CO2 storage. *Water resources research*, *42*(12).

823   Knauss, K.G. and Wolery, T.J., 1986. Dependence of albite dissolution kinetics on pH and time
824   at 25 C and 70 C. *Geochimica et Cosmochimica Acta*, *50*(11), pp.2481-2497.

825   Liu, S.K., Han, C., Liu, J.M. and Li, H., 2015. Hydrothermal decomposition of potassium
826   feldspar under alkaline conditions. *Rsc Advances*, *5*(113), pp.93301-93309.

827   Lu, P., Fu, Q., Seyfried Jr, W. E., Hedges, S. W., Soong, Y., Jones, K., Zhu, C., 2013.
828   Coupled alkali feldspar dissolution and secondary mineral precipitation in batch systems–2:
829   New experiments with supercritical CO2 and implications for carbon sequestration. Appl.
830   Geochem. 30, 75–90.

831 Ma, X., Ma, H. and Yang, J., 2016. Sintering preparation and release properties of K2MgSi3O8

832 slow-release fertilizer using biotite acid-leaching residues as silicon source. *Industrial &*

833 *Engineering Chemistry Research*, *55*(41), pp.10926-10931.

834 Moore, J., Adams, M., Allis, R., Lutz, S. and Rauzi, S., 2005. Mineralogical and geochemical

835 consequences of the long-term presence of CO_2 in natural reservoirs: an example from the

836 Springerville–St. Johns Field, Arizona, and New Mexico, USA. *Chemical geology*, *217*(3-4),

837 pp.365-385.

838 Mora, C.I., Riciputi, L.R., Cole, D.R. and Walker, K.D., 2009. High-temperature hydrothermal

839 alteration of the Boehls Butte anorthosite: origin of a bimodal plagioclase

840 assemblage. *Contributions to Mineralogy and Petrology*, *157*(6), pp.781-795.

841 Neusser, G., Abart, R., Fischer, F.D., Harlov, D. and Norberg, N., 2012. Experimental Na/K

842 exchange between alkali feldspar and an NaCl–KCl salt melt: chemically induced fracturing

843 and element partitioning. *Contributions to Mineralogy and Petrology*, *164*(2), pp.341-358.

844 Niedermeier, D.R., Putnis, A., Geisler, T., Golla-Schindler, U. and Putnis, C.V., 2009. The

845 mechanism of cation and oxygen isotope exchange in alkali feldspars under hydrothermal

846 conditions. *Contributions to Mineralogy and Petrology*, *157*(1), pp.65-76.

847 Norberg, N., Neusser, G., Wirth, R. and Harlov, D., 2011. Microstructural evolution during

848 experimental albitization of K-rich alkali feldspar. *Contributions to Mineralogy and*

849 *Petrology*, *162*(3), pp.531-546.

850 Pinnock, S.J., Clitheroe, A.R.J. and Rose, P.T.S., 2003. The Captain Field, Block 13/22a, UK

851 North Sea.

852 Putnis, A., 2009. Mineral replacement reactions. *Reviews in mineralogy and*

853 *geochemistry*, *70*(1), pp.87-124.

854 Rathnaweera, T.D., Ranjith, P.G., Perera, M.S.A., Haque, A., Lashin, A., Al Arifi, N.,

855 Chandrasekharam, D., Yang, S.Q., Xu, T., Wang, S.H. and Yasar, E., 2015. CO_2-induced

856 mechanical behaviour of Hawkesbury sandstone in the Gosford basin: An experimental

857 study. *Materials Science and Engineering: A*, *641*, pp.123-137.

858 Ringrose, P., 2020. How to store CO_2 underground: Insights from early-mover CCS projects.

859 Rochelle, C.A., Czernichowski-Lauriol, I. and Milodowski, A.E., 2004. The impact of

860 chemical reactions on CO_2 storage in geological formations: a brief review.

861   Ross, G.D., Todd, A.C., Tweedie, J.A. and Will, A.G., 1982, April. The dissolution effects of

862   CO2-brine systems on the permeability of UK and North Sea calcareous sandstones. In *SPE*

863   *Improved Oil Recovery Conference?* (pp. SPE-10685). SPE.

864   Rutter, E.H., 1976. A discussion on natural strain and geological structure-the kinetics of rock

865   deformation by pressure solution. *Philosophical Transactions of the Royal Society of London.*

866   *Series A, Mathematical and Physical Sciences*, *283*(1312), pp.203-219.

867   Scholz, C.H., 1972. Static fatigue of quartz. *Journal of Geophysical Research*, *77*(11),

868   pp.2104-2114.

869   Seisenbayev, N., Absalyamova, M., Alibekov, A. and Lee, W., 2023. Reactive transport

870   modeling and sensitivity analysis of CO2–rock–brine interactions at Ebeity Reservoir, West

871   Kazakhstan. *Sustainability*, *15*(19), p.14434.

872   Shell, 2015. 'Peterhead CCS Project: Geochemical Reactivity Report CCS-05-PT-ZR-3323-

873   00001. PVT Modelling Report for CO2 in Goldeneye Project

874   Shogenov, K., Shogenova, A., Vizika-Kavvadias, O. and Nauroy, J.F., 2015. Experimental

875   modeling of CO2-fluid-rock interaction: The evolution of the composition and properties of

876   host rocks in the Baltic Region. *Earth and Space Science*, *2*(7), pp.262-284.

877   Stewart, N. and Marshall, J.D., 2020. The Goldeneye Field, Blocks 14/29a and 20/4b, UK

878   North Sea.

879   Summers, R. and Byerlee, J., 1977, May. A note on the effect of fault gouge composition on

880   the stability of frictional sliding. In *International Journal of Rock Mechanics and Mining*

881   *Sciences & Geomechanics Abstracts* (Vol. 14, No. 3, pp. 155-160). Pergamon.

882   Tullis, J. and Yund, R.A., 1977. Experimental deformation of dry Westerly granite. *Journal of*

883   *geophysical research*, *82*(36), pp.5705-5718.

884   Wigley, M., Dubacq, B., Kampman, N. and Bickle, M., 2013. Controls of sluggish, CO2-

885   promoted, hematite and K-feldspar dissolution kinetics in sandstones. *Earth and Planetary*

886   *Science Letters*, *362*, pp.76-87.

887   Whitney, D.L. and Evans, B.W., 2010. Abbreviations for names of rock-forming

888   minerals. *American mineralogist*, *95*(1), pp.185-187.

889   Wollast, R., 1967. Kinetics of the alteration of K-feldspar in buffered solutions at low

890   temperature. *Geochimica et Cosmochimica Acta*, *31*(4), pp.635-648.

891   Wheeler, J., 1991. A view of texture dynamics. *Terra Nova*, *3*(2), pp.123-136.

892   Whitney, D.L., Evans, B.W., 2010. Abbreviations for names of rock-forming minerals.

893   Amer. Mineral. 95, 185–187.

894   YuanYuan, Z., QingDong, Z., Roland, H., ShanKe, L., JianMing, L. and JingBo, N., 2020.

895   Reaction mechanism during hydrothermal alteration of K-feldspar under alkaline conditions

896   and nanostructures of the produced tobermorite. *Acta Petrologica Sinica*, *36*(9), pp.2834-

897   2844.

898   Zeitler, P.K., Enkelmann, E., Thomas, J.B., Watson, E.B., Ancuta, L.D. and Idleman, B.D.,

899   2017. Solubility and trapping of helium in apatite. *Geochimica et Cosmochimica Acta*, *209*,

900   pp.1-8.

901   Zhai, Y., Hellmann, R., Campos, A., Findling, N., Mayanna, S., Wirth, R., Schreiber, A.,

902   Cabié, M., Zeng, Q., Liu, S. & Liu, J., 2021. Fertilizer derived from alkaline hydrothermal

903   alteration of K-feldspar: micrometer to nanometer-scale investigation. *Applied Geochemistry*,

904   126, p.104828.

905